



Article

Nanoparticulate Perovskites for Photocatalytic Water Reduction

Sven A. Freimann, Catherine E. Housecroft and Edwin C. Constable *

Department of Chemistry, University of Basel, Mattenstrasse 22, BPR 1095, Postfach, 4002 Basel, Switzerland; catherine.housecroft@unibas.ch (C.E.H.)

* Correspondence: edwin.constable@unibas.ch

Abstract: SrTiO₃ and BaTiO₃ nanoparticles (NPs) were activated using H₂O₂ or aqueous HNO₃, and pristine and activated NPs were functionalized with a 2,2'-bipyridine phosphonic acid anchoring ligand (1), followed by reaction with RuCl₃·3H₂O and bpy, RhCl₃·3H₂O and bpy, or RuCl₃·3H₂O. The surface-bound metal complex functionalized NPs were used for the photogeneration of H₂ from water, and their activity was compared to related systems using TiO₂ NPs. The role of pH during surface complexation was found to be important. The NPs were characterized using Fourier transform infrared (FTIR) and solid-state absorption spectroscopies, thermogravimetric analysis mass spectrometry (TGA-MS), and matrix-assisted laser desorption/ionization mass spectrometry (MALDI-MS), and the dihydrogen generation was analyzed using gas chromatography–mass spectrometry (GC-MS). Our findings indicate that extensively functionalized SrTiO₃ or BaTiO₃ NPs may perform better than TiO₂ NPs for water reduction.

Keywords: nanoparticles; anchored catalyst; heterogeneous catalysis; water reduction



Citation: Freimann, S.A.; Housecroft, C.E.; Constable, E.C. Nanoparticulate Perovskites for Photocatalytic Water Reduction. *Nanomaterials* **2023**, *13*, 2094. <https://doi.org/10.3390/nano13142094>

Academic Editors: Botao Teng and Detlef Bahnemann

Received: 28 June 2023

Revised: 11 July 2023

Accepted: 15 July 2023

Published: 18 July 2023



Copyright: © 2023 by the authors. Licensee MDPI, Basel, Switzerland. This article is an open access article distributed under the terms and conditions of the Creative Commons Attribution (CC BY) license (<https://creativecommons.org/licenses/by/4.0/>).

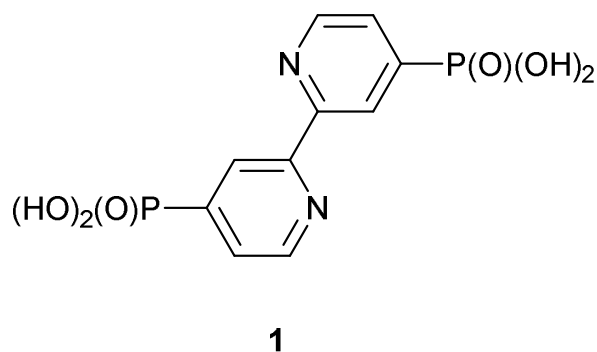
1. Introduction

Increasing global economic development and a growing population have resulted in a higher demand for energy [1]. The burning of fossil fuels to provide energy releases greenhouse gases, which places immense stress on the environment. In the long term, this will cost society increasing amounts of resources [2–5]. As a consequence, research focusing on inexpensive energy solutions is increasingly focused on renewable and clean sources [6]. One solution is the use of dihydrogen derived from renewable sources as fuel or energy storage [7]. An attractive approach to a hydrogen economy is to combine energy harvesting and H₂ evolution using photocatalysts operating under solar irradiation [8]. Hence, the design and development of efficient photocatalysts are crucial. A major contribution to this development is the use of heterogeneous catalysts [9–12]. These are often easier to recover than homogeneous catalysts but have the disadvantage of inactive interior volumes, with only surface sites being catalytically active [13–15]. An alternative is functionalizing nanoparticle (NP) scaffolds with photocatalysts. Such immobilized photocatalysts offer greater catalyst-to-volume ratios than bulk heterogeneous catalysts, and this enhances the catalytic activity and turnover. An additional benefit of NPs is the possibility of dispersing them in liquid phases [16–19].

In previous studies, we have shown that the binding of photo- and redox-active Rh and Ru coordination compounds onto TiO₂ NP surfaces can be used successfully for H₂ production, with the catalytic activity of the NP-supported catalyst outperforming previously reported, related homogeneous catalysts [20]. Another promising class of photocatalysts are perovskite-type oxides MTiO₃ (M = Ca, Sr or Ba). These comprise cheap, earth-abundant elements [21–23], are water-insoluble, thermodynamically stable, and resistant to temperature- and photo-corrosion [24]. The photocatalytic properties of MTiO₃ can be improved, tuned, and modified. This has been demonstrated using alternative synthetic methods [25,26], doping with organic or inorganic compounds [24,27,28], surface nanoparticle deposition [29,30], the use of cocatalysts [31,32], or the use of composites [33,34].

The photocatalytic properties of perovskites have been utilized for several applications, including organic compound degradation (methylene blue [24,25], methylene orange [29], salicylic acid [35], or ofloxacin dyes [34]) or H₂ generation. In particular, SrTiO₃ and BaTiO₃ offer excellent activity in H₂ generation. For example, the use of doped SrTiO₃ has been widely demonstrated with examples, including Mn-, Ru-, Rh-, Ir- [27], Na- [36], Al-La- [37], and La-Rh- dopants [38]. Further approaches that result in improved H₂ generation with doped SrTiO₃ involve the introduction of oxygen vacancies [39] or additional cocatalysts, including Na-SrTiO₃ combined with Rh_{2-y}Cr_yO₃ [31] or Al-SrTiO₃ with RhCrO_x [32]. Similarly, BaTiO₃ has been doped with Rh and functionalized with Pt nanoparticles to give a composite material shown to generate H₂ upon irradiation [40]. A further promising feature of SrTiO₃ and BaTiO₃ NPs is their relatively similar pH-dependent zeta potentials and band gaps, only ~0.2 eV larger than TiO₂ [41–46]. Functionalization using various anchoring groups, including phosphonic acids, carboxylic acids, or even hydroxy groups, makes them suitable candidates to extend our earlier results obtained with TiO₂ NPs [47,48].

In this work, we report the surface activation of pristine SrTiO₃ and BaTiO₃ NPs using either HNO₃ or H₂O₂. The activated NPs are abbreviated as SrTiO₃-a, BaTiO₃-a (HNO₃ activation) or SrTiO₃-OH, BaTiO₃-OH (H₂O₂ activation), respectively. We compare the subsequent functionalization of each type of pristine and activated NP with the ligand [2,2'-bipyridine]-4,4'-diylbis(phosphonic acid) (**1**, Scheme 1) which contains phosphonic acid anchoring domains. The functionalized NPs were used for direct surface metal complex assembly by reaction with 2,2'-bipyridine (bpy) and ruthenium or rhodium trichloride to give a surface-bound complex presumed to be (but not established as) an [M(bpy)₂(**1**)]-species. The photocatalytic behavior of these metal-functionalized NPs was investigated. Experiments were also conducted to highlight the importance of pH control for successful metal complex assembly on the NP surface. The NPs were characterized using Fourier transform infrared (FTIR) and solid-state absorption spectroscopies, thermogravimetric analysis mass spectrometry (TGA-MS), and matrix-assisted laser desorption/ionization mass spectrometry (MALDI-MS), and the dihydrogen generation was analyzed using gas chromatography–mass spectrometry (GC-MS).



Scheme 1. Anchoring ligand **1**.

2. Materials and Methods

2.1. General

RuCl₃·3H₂O and RhCl₃·3H₂O were purchased from Oxkem Ltd. (Reading, UK) and Johnson Matthey (Materials Technology, Reading, UK). 2,2'-Bipyridine (bpy) and triethanolamine (TEOA) were purchased from Apollo Scientific Ltd. (Stockport, UK) and Sigma Aldrich Chemie GmbH (Buchs, Switzerland), respectively. K₂[PtCl₄] was purchased from Alfa Aesar GmbH & Co KG (Karlsruhe, Germany). Pristine SrTiO₃ and BaTiO₃ NPs were purchased from Sigma-Aldrich Chemie GmbH (Buchs, Switzerland) and had diameter sizes of <100 and 50 nm, respectively; further characterizations are reported in the Supplementary Materials. The anchoring ligand **1** was prepared as previously described [20]. Instrumentation details are given in the Supplementary Materials. The

calculated major MALDI peaks reported in the Supplementary Materials were determined using the most abundant isotopes (e.g., ^{102}Ru , ^{35}Cl). For functionalized NPs in which the surface-bound ligand **1** is coordinated to a metal, a simplified notation is introduced; for example, Ru@SrTiO_3 describes a SrTiO_3 NP modified with ligand **1** which is also coordinated to Ru. In the case of NPs functionalized with both Ru and Rh, the relative amounts of the two metals are indicated using lower case (lower concentration) or upper case (higher concentration) letters (**r** or **R**). The first letter refers to Ru and the second to Rh, e.g., rR@SrTiO_3 describes metal complex-functionalized NPs with Ru/Rh in a 1:20 molar ratio on the surface.

2.2. Experimental

2.2.1. Nanoparticle Surface Activation Using HNO_3 ($\text{SrTiO}_3\text{-a}$, $\text{BaTiO}_3\text{-a}$)

Pristine SrTiO_3 or BaTiO_3 NPs were activated as previously reported [20]. The NPs (2.00 g) were dispersed by sonication for 15 min in dilute aqueous HNO_3 (30 mL, 3.0 M). The mixture was then stirred for 30 min. The suspension was centrifuged (10 min, 7000 rpm) and the NPs were washed once with milliQ water (40 mL). The NPs were added to milliQ water (40 mL) and dispersed by sonication for 10 min. The suspension was then stirred for 72 h. The suspension was centrifuged (10 min, 7000 rpm), and the NPs were washed with milliQ water (2×40 mL). The activated NPs ($\text{SrTiO}_3\text{-a}$, 1.67 g and $\text{BaTiO}_3\text{-a}$, 0.60 g) were stored in a sealed vial under N_2 after drying them under high vacuum. The characterization data of the pristine NPs and acid-activated NPs are given in the Supplementary Materials. The TGA and TGA-MS spectra of the pristine NPs (Figures S1–S4) and acid-activated NPs (Figures S5–S7) are given in the Supplementary Materials.

2.2.2. Nanoparticle Surface Activation Using H_2O_2 ($\text{SrTiO}_3\text{-OH}$, $\text{BaTiO}_3\text{-OH}$)

Pristine SrTiO_3 or BaTiO_3 NPs were activated as reported in the literature [49]. The NPs (1.05 g) were dispersed by sonication for 20 min in H_2O_2 (50 mL, 30%). The mixture was then stirred for 4 h at 110 °C under N_2 . The suspension was cooled down, centrifuged (10 min, 7000 rpm), and the NPs were washed with milliQ water (40 mL). The activated NPs (1.05 g and 1.05 g) were stored in a sealed vial under N_2 after drying them under high vacuum for 72 h. The characterization data are given in the Supplementary Materials. The TGA and TGA-MS spectra of the H_2O_2 -activated NPs (Figures S8–S11) are given in the Supplementary Materials.

2.2.3. Nanoparticle Surface Ligand Functionalization (1@SrTiO_3 , $1\text{@SrTiO}_3\text{-a}$, $1\text{@SrTiO}_3\text{-OH}$, 1@BaTiO_3 , $1\text{@BaTiO}_3\text{-a}$, $1\text{@BaTiO}_3\text{-OH}$)

The functionalization was performed as previously reported [20]. Anchoring ligand **1** (10.0 mg, 31.6 μmol , 1.0 eq.) and milliQ water (18 mL) were added to a microwave vial and dispersed by sonication for 1 min. Acid- or H_2O_2 -activated NPs (449.0 mg, 4.6 SrTiO_3 eq. or 7.3 BaTiO_3 eq.) were added. The suspension was dispersed by sonication for 10 min. The microwave vial was sealed, and the reaction mixture was heated for 3 h at 130 °C in the microwave reactor. After cooling to room temperature, the suspension was centrifuged (20 min, 7000 rpm). The NPs were separated from the solvent and washed with EtOH (2×15 mL). This procedure gave white f-NPs (f-NP = functionalized NP) with the following yields: $1\text{@SrTiO}_3\text{-a}$ NPs (418.3 mg), $1\text{@SrTiO}_3\text{-OH}$ NPs (422.6 mg), $1\text{@BaTiO}_3\text{-a}$ NPs (409.9 mg), $1\text{@BaTiO}_3\text{-OH}$ NPs (425.1 mg), and these were stored in a sealed vial under N_2 after drying the NPs under high vacuum. This reaction was repeated using pristine SrTiO_3 and BaTiO_3 NPs (224 mg, 4.6 SrTiO_3 eq. or 7.3 BaTiO_3 eq.) and **1** (5.0 mg, 15.8 μmol) yielding 1@SrTiO_3 NPs (218.1 mg, 221.6 mg) and 1@BaTiO_3 NPs (210.7 mg, 219.4 mg). For NMR spectroscopic measurements, NPs (5–10 mg) were dispersed in 500 μL D_2O in an NMR tube. The characterization data are given in the Supplementary Materials. The TGA, TGA-MS, and MALDI spectra of the pristine (Figures S12–S17), acid-activated (Figures S18–S22), and H_2O_2 -activated (Figures S23–S28) functionalized NPs are given in the Supplementary Materials.

2.2.4. Nanoparticle Surface Complexation (**Ru@SrTiO₃**, **Ru@BaTiO₃**)

The metal complex was formed directly on the NP surface. **1@SrTiO₃** (70.9 mg), RuCl₃·3H₂O (1.03 mg, 3.94 μmol), and bpy (1.25 mg, 8.00 μmol) were added to a vial. H₂O (5.0 mL) and EtOH (3.0 mL) were added, and the mixture was thoroughly dispersed using sonication and stirring. The suspension was transferred into an autoclave PTFE liner with additional EtOH (2.0 mL). The autoclave was sealed and then heated in an oven at a heating rate of 320 °C/h to 160 °C. The autoclave was left at 160 °C for 1 h. After cooling, the autoclave was opened, and the suspension was centrifuged (20 min, 7000 rpm). The resulting NPs were washed with H₂O (3 × 10 mL) and EtOH (1 × 10 mL). **Ru@SrTiO₃** (65.8 mg) was obtained as a pale orange powder after drying the NPs under a high vacuum. This experiment was repeated with **1@BaTiO₃** (70.9 mg), RuCl₃·3H₂O (1.03 mg, 3.95 μmol), and bpy (1.25 mg, 8.00 μmol) yielding **Ru@BaTiO₃** (67.0 mg) as a dark brown powder. The characterization data are given in the Supplementary Materials. The TGA, TGA-MS, and MALDI spectra are given in the Supplementary Materials (Figures S29–S34).

2.2.5. Nanoparticle Surface Complexation (**rR@SrTiO₃**, **rR@SrTiO₃-a**, **rR@SrTiO₃-OH**, **rR@SrTiO₃-OH-A**, **rR@BaTiO₃**, **rR@BaTiO₃-a**, **rR@BaTiO₃-OH**, **rR@BaTiO₃-OH-A**)

The notation is defined in Section 2.1. The metal complex was formed directly on the NP surface. This reaction was carried out with each isolated NP from Sections 2.2.1 and 2.2.2. Hence, **1@SrTiO₃**, **1@SrTiO₃-a** NPs, **1@SrTiO₃-OH**, **1@BaTiO₃**, **1@BaTiO₃-a**, or **1@BaTiO₃-OH** (365.6 mg) was added to a vial with RuCl₃·3H₂O (0.24 mg, 0.9 μmol), RhCl₃·3H₂O (5.15 mg, 19.6 μmol), and bpy (6.45 mg, 41.3 μmol). H₂O (5.0 mL) and EtOH (3.0 mL) were added, and the mixture was thoroughly dispersed using sonication and stirring. The suspension was transferred to an autoclave with a PTFE liner with additional EtOH (2.0 mL). The autoclave was sealed and then heated in an oven at a rate of 320 °C/h to 160 °C. The autoclave was left at 160 °C for 1 h. After cooling, the autoclave was opened, and the suspension was centrifuged (20 min, 7000 rpm). The resulting NPs were washed with H₂O (3 × 10 mL) and EtOH (1 × 10 mL). After drying the NPs under high vacuum, the reaction yielded **rR@SrTiO₃** (354.2 mg) as a pale orange powder, **rR@SrTiO₃-a** (358.2 mg) as a pale orange powder, **rR@SrTiO₃-OH** (358.4 mg) as a grey powder, **rR@BaTiO₃** (349.9 mg) as a grey powder, **rR@BaTiO₃-a** (356.9 mg) as a dark brown powder or **rR@BaTiO₃-OH** (357.4 mg) as a dark grey powder. This reaction was repeated with **1@SrTiO₃-OH** and **1@BaTiO₃-OH** with a pH adjusted to 1.5 using 4.0 mL H₂O, 1.0 mL aqueous H₂SO₄ (1 M), and the same amount of EtOH (5 mL). Other reaction conditions were kept the same. **rR@SrTiO₃-OH-A** (356.0 mg) and **rR@BaTiO₃-OH-A** (355.1 mg) were both isolated as a pale orange powder. The characterization data are given in the Supplementary Materials. The TGA, TGA-MS, and MALDI spectra of the pristine (Figures S36–S40), acid-activated (Figures S41–S45), H₂O₂-activated (Figures S46–S51), and H₂O₂-activated under adjusted pH (Figures S52–S55) functionalized, and ruthenium-, rhodium-, and bpy-complexed NPs are given in the Supplementary Materials. An FTIR reference spectrum (Figure S56) was recorded by mixing pristine SrTiO₃ NPs (500 mg) with aqueous H₂SO₄ (200 μL, 3 M) using a mortar.

2.2.6. Dihydrogen Generation

The water reduction reaction conditions were consistent with the conditions in the previous work with TiO₂ NPs [20]. Triethanolamine (TEOA) was added as a sacrificial electron donor, K₂[PtCl₄] as a catalyst to facilitate H₂ formation (feasibly by the formation of Pt nanoparticles), bpy as an additive, aqueous H₂SO₄ for altering the solution pH. TEOA (2.52 mmol, 376 mg), K₂[PtCl₄] (1.7 μmol, 0.70 mg), and bpy (18.6 μmol, 2.91 mg) were added to a 5 mL microwave vial with milliQ water and aqueous H₂SO₄ (1 M) to modify the pH. The experiments were performed at pH 7.5 and used 1 mL aqueous H₂SO₄ (1 M) and 5 mL milliQ water. Metal complex-functionalized NPs were added (114.1 mg). The vial was flushed with N₂ and then sealed. The suspension was sonicated (10 min) and thoroughly shaken. N₂ was bubbled through the suspension for 10 min. The vial was irradiated using

a sun simulator generating 1200 W m^{-2} (see the Supplementary Materials) for 4 h with an incident angle of light of 5° . The suspension was stirred throughout the irradiation and periodically shaken. Headspace samples for gas chromatography were collected using a syringe and transferred to a 10 mL GC vial for analysis. The measured GC integral was converted into mL of H_2 with calibration performed by injecting several known volumes of H_2 .

3. Results and Discussion

3.1. NP Activation, Functionalization, Surface Complexation, and Material Characterization

3.1.1. NP Surface Activation

The surface activation of NPs is a crucial step for successful and stable surface functionalization. We previously described the benefits of acid activation of TiO_2 NPs for their use in catalysis [20]. However, in the literature, other methods are also described, including using various acids (e.g., MeCO_2H or HF), hydrogen peroxide, or plasma for surface activation [49–51]. These methods are used to enhance the surface reactivity and make the surface more reactive for functionalization. TiO_2 and SrTiO_3 NPs are acid-resistant, whereas BaTiO_3 NPs are sensitive to mineral acids. Hence, as described in Section 2.2.1, during acid activation with aqueous HNO_3 (3 M), the BaTiO_3 NPs partially dissolved or were lost during washing (70%). Since acid activation was unsuitable for the BaTiO_3 NPs, other activation methods were explored, and activation using the H_2O_2 treatment [49] was chosen. This method simultaneously saturates the surface with hydroxyl groups and strips it of carbonate groups. Although the literature protocol required hydroxyl groups for a salinization reaction [49], the hydroxyl groups should also favor condensation with the phosphonic acid of the anchoring ligand.

Activation was performed with both SrTiO_3 and BaTiO_3 by boiling the dispersed NPs under N_2 in 30% H_2O_2 . The particles were washed with water and then dried for 72 h under high vacuum. The pristine and activated NPs were characterized using FTIR and TGA-MS. The FTIR differences shown in Figure 1 were limited to the fingerprint region. For the pristine SrTiO_3 activated with H_2O_2 , an additional absorption at 1446 cm^{-1} appeared. The pristine BaTiO_3 activated with acid showed the disappearance of a prominent peak at 1420 cm^{-1} , while the activation with H_2O_2 caused the peak to shift and broaden.

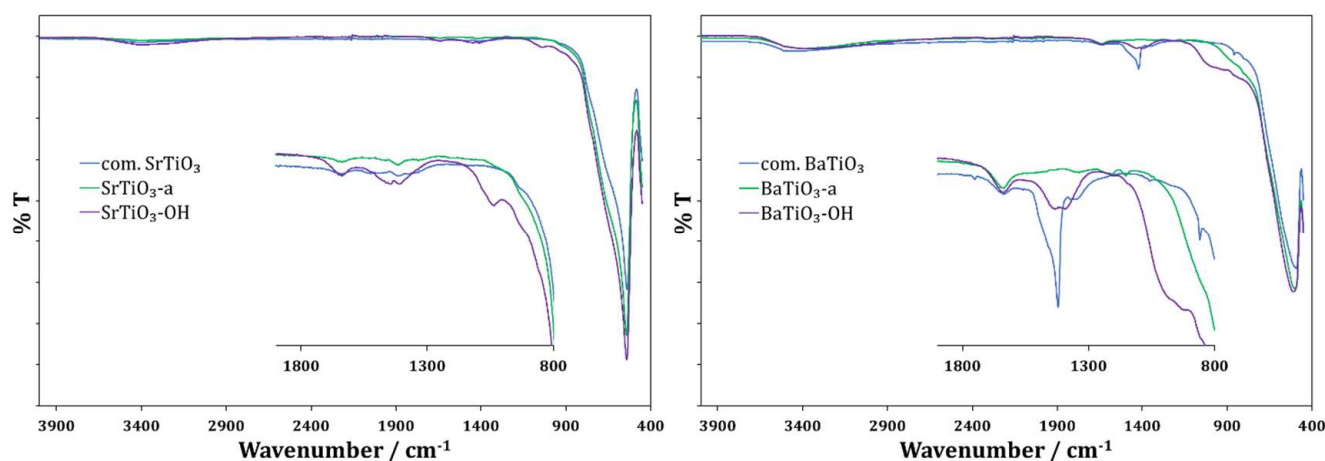


Figure 1. FTIR spectra of pristine SrTiO_3 NPs (left, blue), $\text{SrTiO}_3\text{-a}$ NPs (left, green), $\text{SrTiO}_3\text{-OH}$ NPs (left, violet); pristine BaTiO_3 (right, blue), $\text{BaTiO}_3\text{-a}$ NPs (right, green), $\text{BaTiO}_3\text{-OH}$ NPs (right, violet).

The TGA-MS results are reported in Table 1. A comparison of the pristine SrTiO_3 and BaTiO_3 NPs with acid-activated NPs (SrTiO_3 and BaTiO_3) shows that there was a slight increase in the weight loss (0.1–0.4%) in the lower temperature region ($<380^\circ\text{C}$). The NPs activated with H_2O_2 showed a greater weight loss than the pristine NPs, with an increase in the lower temperature region of 1.2% or 2.2% for SrTiO_3 and BaTiO_3 . Using

TGA-MS, a peak with amu 18 (H_2O) was found in each sample and assigned to physisorbed and chemisorbed water. For H_2O_2 -activated NPs, this increase could also be due to the loss of the hydroxyl groups. The pristine NPs and H_2O_2 -activated NPs showed organic decomposition products (amu 44, CO_2) throughout the TGA experiment, possibly due to impurities in the pristine samples; this was especially visible for BaTiO_3 .

Table 1. TGA-MS results of non-activated and activated SrTiO_3 and BaTiO_3 NPs. (-a) represents HNO_3 -activated NPs and (-OH) represents H_2O_2 -activated NPs.

Entry	30–380 °C /%	Mass Found /amu	380–900 °C /%	Mass Found /amu
Pristine SrTiO_3	0.5	18; 44 ^a	0.4	18; 44
SrTiO_3 -a	0.6	18	1.0	18, 44 ^b , 81 ^b
SrTiO_3 -OH	1.8	18; 44	0.6	18; 44
Pristine BaTiO_3	1.0	18; 44	0.6	18; 44
BaTiO_3 -a	1.4	18	0.5	18; 44 ^b
BaTiO_3 -OH	3.6	18; 44	0.8	18; 44

^a Peak with amu 44 was recorded as traces slightly above baseline. ^b Peak with amu 44 was only recorded within a temperature range of 500–600 °C.

In the higher temperature region (380–900 °C), H_2O_2 -activated SrTiO_3 and BaTiO_3 NPs also showed slightly higher weight losses (0.2%) than the pristine NPs. The acid-activated SrTiO_3 and BaTiO_3 NPs showed slightly higher (0.6%) and lower (0.1%) weight losses, respectively. In both cases, the TGA-MS experiment recorded a significant weight loss at ~550 °C attributed to amu 44 (CO_2), and, in the case of SrTiO_3 -a, a mass loss at amu 81 was also observed. The TGA-MS experiment on SrTiO_3 -a is illustrated in Figure 2 as an example of the sharp weight loss. The origin of this weight loss is unclear.

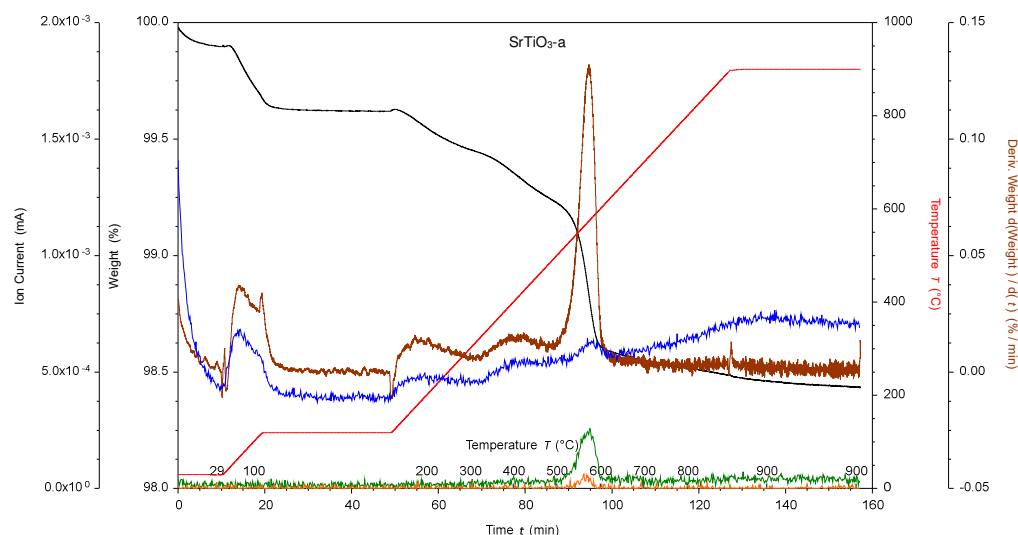


Figure 2. TGA-MS of acid-activated SrTiO_3 NPs. SrTiO_3 -a, where black is the weight loss, red is the temperature, brown is the derivative weight against time, blue is the ion current of amu 18, green is the ion current of amu 44, and orange is the ion current of amu 81.

3.1.2. Nanoparticle Surface Ligand Functionalization

The bpy metal-binding domain in ligand **1** (Scheme 1) was chosen for the surface assembly of $\{\text{M}(\text{bpy})_3\}^{n+}$ ($\text{M} = \text{Ru}$, $n = 2$; $\text{M} = \text{Rh}$, $n = 3$) moieties. Phosphonic acids bind strongly to BaTiO_3 NP surfaces [47], and it is reasonable to assume a similar behavior with SrTiO_3 NPs. The pristine BaTiO_3 and SrTiO_3 NPs had 50 and 100 nm diameters, respectively, making them larger than the p25 TiO_2 NPs used in previous work [20,52,53]. This difference significantly changes the surface area from a volume ratio of 0.28 nm^{-1} for TiO_2 to 0.12 nm^{-1} and 0.06 nm^{-1} for BaTiO_3 and SrTiO_3 , respectively. This reduces

the available surface area and necessitates functionalization adjustments to avoid the free ligand's physisorption. Section 2.2.3 details the functionalization methods adopted. The NPs were characterized using ^1H NMR spectroscopy, FTIR, TGA-MS, MALDI-MS, and solid-state absorption spectroscopy. The TGA-MS results are presented in Table 2 and show higher weight losses than the corresponding unfunctionalized NPs in the high-temperature region (380–900 °C), indicating successful surface functionalization. When compared to TiO_2 , the weight loss due to functionalization was smaller (0.2–0.7% versus 2.6%) [20] than expected since the SrTiO_3 and BaTiO_3 NPs had considerably larger particle sizes. The NPs all showed carbon-containing impurities before functionalization, as described in Section 3.1.1. Based on the TGA-MS experiments in the low-temperature region, the impurities were lost during the functionalization. Figure 3 shows the TGA-MS measurement of $1@\text{SrTiO}_3\text{-a}$, where ligand **1** was decomposed in a single event distinct from the decompositions recorded in the starting material. The TGA-MS measurement of $1@\text{SrTiO}_3$ still shows the peak observed for $\text{SrTiO}_3\text{-a}$ at ~ 550 °C with an additional weight loss between 700 °C and 880 °C. The TGA-MS in this region shows amu 18 (H_2O) and 44 (CO_2), corresponding to a decomposition of the anchoring ligand **1**.

Table 2. TGA-MS results of $1@\text{SrTiO}_3$ and $1@\text{BaTiO}_3$ NPs using non-activated and activated NPs.

Entry	30–380 °C /%	Mass Found /amu	380–900 °C /%	Mass Found /amu
$1@\text{SrTiO}_3$	0.8	18	1.0	18; 44
$1@\text{SrTiO}_3\text{-a}$	0.6	18	1.2	18; 44; 81
$1@\text{SrTiO}_3\text{-OH}$	1.6	18	1.3	18; 44
$1@\text{BaTiO}_3$	1.4	18	1.0	18; 44
$1@\text{BaTiO}_3\text{-a}$	1.5	18	1.2	18; 44; 81
$1@\text{BaTiO}_3\text{-OH}$	3.3	18	1.5	18; 44

(1@) represents ligand **1** bound to the NP surface, (-a) represents using HNO_3 -activated NPs during the functionalization, and (-OH) represents using H_2O_2 -activated NPs during the functionalization.

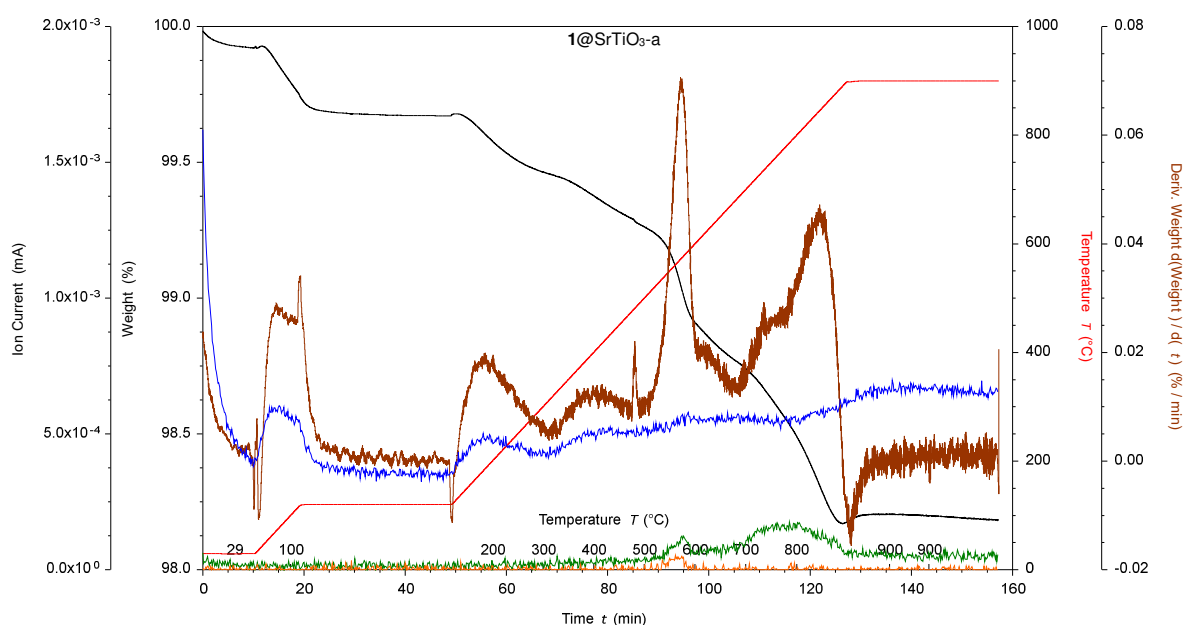


Figure 3. TGA-MS of acid-activated with ligand **1**-functionalized SrTiO_3 NPs. $1@\text{SrTiO}_3\text{-a}$, where black is the weight loss, red is the temperature, brown is the derivative weight against time, blue is the ion current of amu 18, green is the ion current of amu 44, and orange is the ion current of amu 81.

The FTIR spectra of the f-NPs (Figure 4) showed a broad, weak absorption around 3300 cm^{-1} , in accordance with the TGA-MS results, supporting the presence of hydroxy groups. The NPs also exhibited a strong absorption at 540 cm^{-1} and 500 cm^{-1} for SrTiO_3

and BaTiO₃, respectively. Compared to the unfunctionalized NPs, 1@SrTiO₃ and 1@BaTiO₃ (independent of prior activation) showed several absorptions in the range 1900 cm⁻¹ to 900 cm⁻¹, indicating a bound ligand. The possibility of traces of an absorbed and labile species being on the NP surface after the functionalization was excluded based on the ¹H NMR spectroscopy.

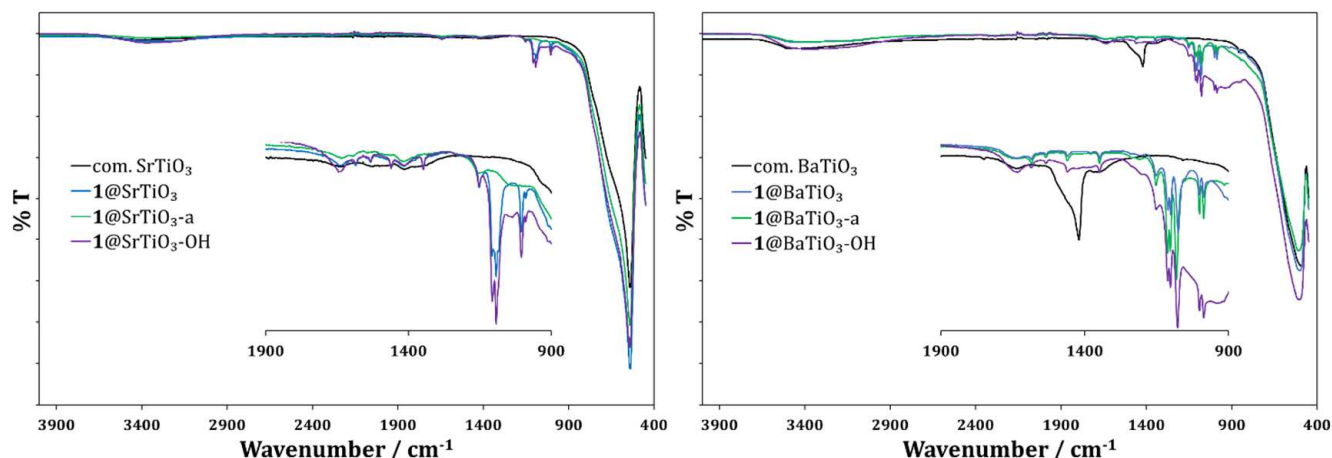


Figure 4. FTIR spectra of pristine SrTiO₃ (left, black), 1@SrTiO₃ NPs (left, blue), 1@SrTiO₃-a NPs (left, green), 1@SrTiO₃-OH NPs (left, violet); pristine BaTiO₃ (right, black), 1@BaTiO₃ NPs (right, blue), 1@BaTiO₃-a NPs (right, green), 1@BaTiO₃-OH NPs (right, violet).

The solid-state absorption spectra used the pristine NPs (SrTiO₃ or BaTiO₃) as the 100% baseline, and the results are shown in Figure 5. The f-NPs showed a broad weak absorption between 400 and 700 nm. These results are similar to the solid-state absorption spectra of the ligand 1-functionalized TiO₂ NPs [20].

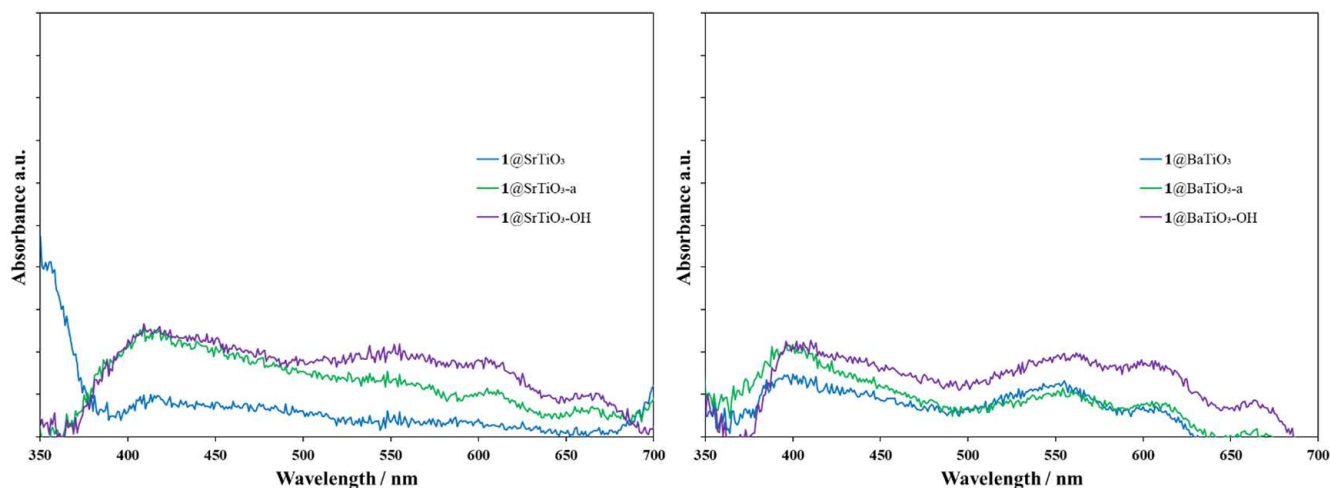


Figure 5. Solid-state absorption spectra of 1@SrTiO₃ NPs (left, blue), 1@SrTiO₃-a NPs (left, green), 1@SrTiO₃-OH NPs (left, violet); 1@BaTiO₃ NPs (right, blue), 1@BaTiO₃-a NPs (right, green), 1@BaTiO₃-OH NPs (right, violet).

3.1.3. Nanoparticle Surface Complexation

For all complexations, the f-NPs were dispersed in an autoclave in a mixture of H₂O/EtOH together with RuCl₃·3H₂O, RhCl₃·3H₂O, and bpy (see Sections 2.2.4 and 2.2.5 for detailed procedures). Depending on the activation of the NPs and the pH during the complexation, differently colored NPs with different catalytic activities were isolated. The ruthenium and rhodium metal complex-bearing NPs were tested for their ability to catalyze

dihydrogen production from water under irradiation using simulated sunlight. The method was also utilized with only $\text{RuCl}_3 \cdot 3\text{H}_2\text{O}$ to prepare Ru@SrTiO_3 and Ru@BaTiO_3 . The isolated f-NPs are shown in Figure 6 and were characterized using ^1H NMR spectroscopy, FTIR, TGA-MS, MALDI-MS, and solid-state absorption spectroscopy.



Figure 6. Isolated f-NPs from left to right: rR@SrTiO_3 , $\text{rR@SrTiO}_3\text{-a}$, $\text{rR@SrTiO}_3\text{-OH}$, $\text{rR@SrTiO}_3\text{-OH-A}$, Ru@SrTiO_3 , Ru@BaTiO_3 , rR@BaTiO_3 , $\text{rR@BaTiO}_3\text{-a}$, $\text{rR@BaTiO}_3\text{-OH}$, $\text{rR@BaTiO}_3\text{-OH-A}$.

TGA-MS revealed an increased weight loss of the complex-bearing NPs when comparing them to ligand-functionalized NPs. The results are shown in Table 3. The greater weight loss for the metal complexed f-NPs compared to the ligand f-NPs in the high-temperature region (380–900 °C) was rather low (0.2–0.5%). This provides evidence for the low degree of functionalization compared to the equivalent functionalized TiO_2 NPs [20].

Table 3. TGA-MS results of rR@SrTiO_3 and rR@BaTiO_3 NPs using non-activated and activated NPs.

Entry	30–380 °C /%	Mass Found /amu	380–900 °C /%	Mass Found /amu
rR@SrTiO_3	0.9	18; 44	1.5	18; 44
$\text{rR@SrTiO}_3\text{-a}$	0.7	18; 44	1.4	18; 44
$\text{rR@SrTiO}_3\text{-OH}$	1.5	18; 44	1.6	18; 44
$\text{rR@SrTiO}_3\text{-OH-A}$	1.2	18	5.3	18; 44; 48; 64
rR@BaTiO_3	0.9	18; 44	1.2	18; 44
$\text{rR@BaTiO}_3\text{-a}$	1.6	18; 44	1.5	18; 44
$\text{rR@BaTiO}_3\text{-OH}$	3.2	18; 44	1.6	18; 44
$\text{rR@BaTiO}_3\text{-OH-A}$	2.9	18	7.6	18; 44; 48; 64

(rR@) represents anchoring ligand 1-f-NPs bound to the surface of the NPs and complexed with RuCl_3 and RhCl_3 at a ratio of roughly 1:20; (-a) represents using HNO_3 activated NPs during the functionalization; (-OH) means H_2O_2 activated NPs during the functionalization; (-OH-A) refers to additionally adjusting the pH to 1.5 during the complexation.

A successful complexation was expected to result in additional decomposition in the TGA-MS. Hence, the TGA-MS data of $\text{SrTiO}_3\text{-a}$ (Figure 2) and $1\text{@SrTiO}_3\text{-a}$ (Figure 3) to $\text{rR@SrTiO}_3\text{-a}$ (Figure 7) were used to identify the decomposition processes. Using the ion current of CO_2 , amu 44 (Figure 7, green), the decompositions can be differentiated from the starting material. The decomposition of $\text{rR@SrTiO}_3\text{-a}$ occurred at a slightly lower temperature (~650 °C) than the recorded decomposition for $1\text{@SrTiO}_3\text{-a}$ (~800 °C) and higher than the impurity recorded with $\text{SrTiO}_3\text{-a}$ (~550 °C).

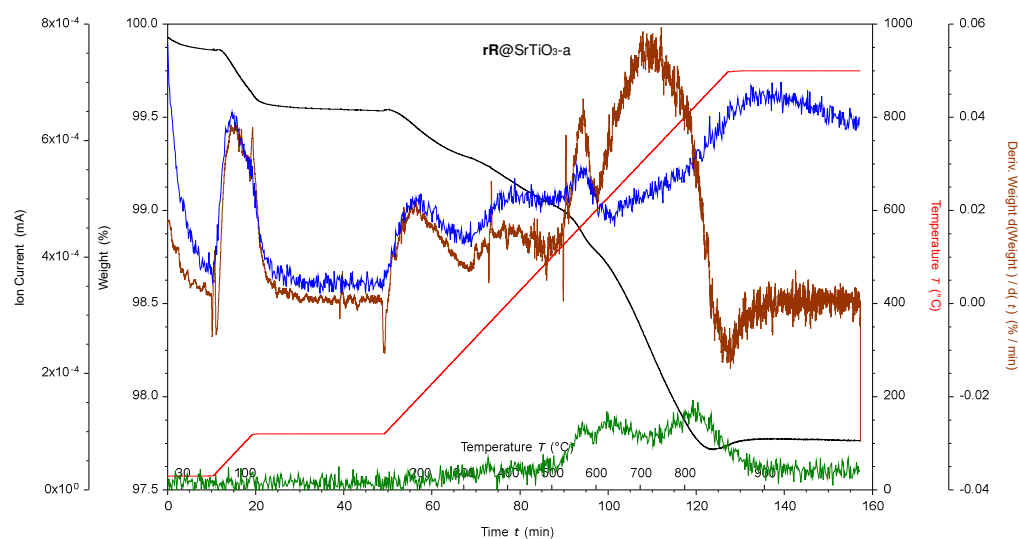


Figure 7. TGA-MS of acid-activated with ligand **1**-functionalized and ruthenium-, rhodium-, and bpy-complexed SrTiO₃ NPs. **rR@SrTiO₃-a**, where black is the weight loss, red is the temperature, brown is the derivative weight against time, blue is the ion current of amu 18, and green is the ion current of amu 44.

In further experiments with **1@SrTiO₃-OH** and **1@BaTiO₃-OH**, the pH for the complexation reaction in the autoclave was adjusted from 6.9 to 1.5 with aqueous H₂SO₄. The resulting NPs showed large weight loss increases in the high-temperature region of 4.0% (Figure 8, bottom, labeled **rR@SrTiO₃-OH-A**) and 6.1% (Figure 8, top, **rR@BaTiO₃-OH-A**). However, the TGA-MS showed peaks at amu 48 (SO) and 64 (SO₂) at 750 °C, suggesting the surface binding of H₂SO₄ [54]. The presence of amu 44 (CO₂, Figure 8) suggests an organic decomposition, indicating that the decomposition of H₂SO₄ was not the main cause of the weight loss. The main weight loss occurred at ~700 °C, corresponding to the decomposition also observed for **rR@SrTiO₃-a**. The earlier decomposition at ~550 °C and ~800 °C was not observed for **rR@SrTiO₃-OH-A**. For **rR@BaTiO₃-OH-A**, an additional decomposition at ~900 °C was observed. ¹H NMR spectroscopy was used to verify the absence of a non-bound anchoring ligand in all cases.

The solid-state absorption spectra of the complexed NPs are shown in Figure 9. In the case of SrTiO₃, the spectrum of the metal complex f-NPs (Figure 9, left) shows a broad absorption between 410 nm and 480 nm, with weaker absorptions between 500 and 700 nm. These generally agree with the absorption spectra for the corresponding TiO₂ NPs [20]. However, **rR@SrTiO₃-OH** NPs (Figure 9, left, violet) exhibited more intense absorptions in the regions 540–570, 600–620, and 660–680 nm. As these NPs were grey to black, a panchromatic absorption was to be expected. Metal complex f-NPs with BaTiO₃ NPs (Figure 9, right) showed similar panchromatic adsorption. For **rR@BaTiO₃-OH-A** (Figure 9, right, red), absorptions between 600–620 and 660–680 nm were less intense than other NPs, in accordance with their pale orange color.

Figure 10 shows the FTIR spectra of **rR@SrTiO₃** (left, blue) and **rR@BaTiO₃** (right, blue) and their variants (-a, green; -OH, violet; -OH-A, red). Overall, the FTIR spectra of all metal complex f-NPs of SrTiO₃ and BaTiO₃ were similar (except for **rR@SrTiO₃-OH-A** and **rR@BaTiO₃-OH-A**). In addition, the spectra were very similar to that of the anchoring ligand f-NPs described in Section 3.1.2, with only small differences in the fingerprint region (1900 to 900 cm⁻¹). In contrast, the FTIR spectra of **rR@SrTiO₃-OH-A** and **rR@BaTiO₃-OH-A** showed strong absorptions at 1219, 1141, and 1100 and at 1200 and 1091 cm⁻¹, respectively, due to the presence of H₂SO₄ on the NP surface. This was confirmed by recording an FTIR spectrum of a mixture of pristine SrTiO₃ NPs and aqueous H₂SO₄ (see Supplementary Materials, Figure S56).

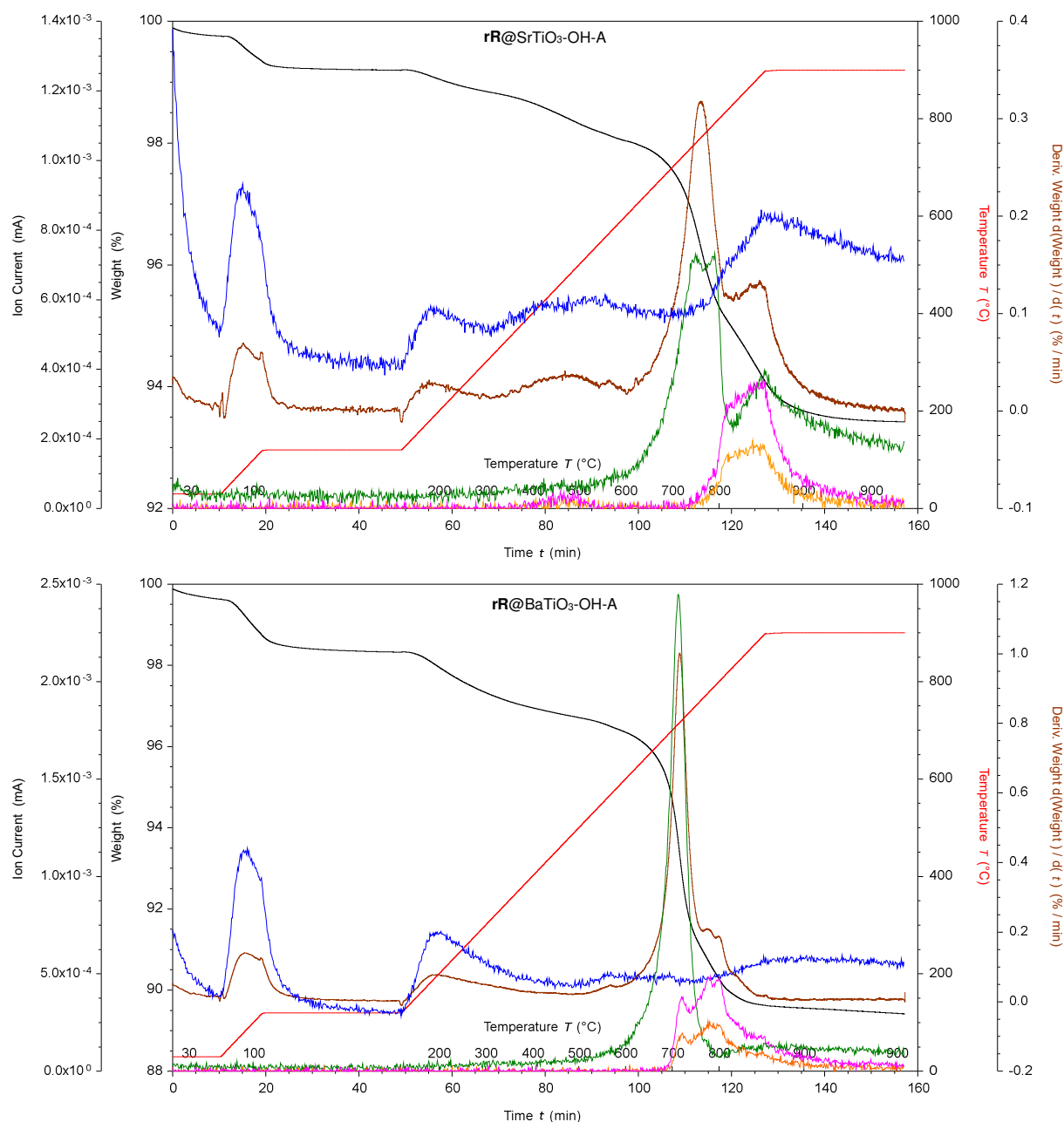


Figure 8. TGA-MS of H_2O_2 activated with ligand **1**-functionalized and ruthenium, rhodium, and bpy under adjusted pH complexed SrTiO_3 NPs (**top**) and BaTiO_3 NPs (**bottom**). $\text{rR@SrTiO}_3\text{-OH-A}$ and $\text{rR@BaTiO}_3\text{-OH-A}$, where black is the weight loss, red is the temperature, brown is the derivative weight against time, blue is the ion current of amu 18, green is the ion current of amu 44, yellow is the ion current of amu 48, and pink is the ion current of amu 64.

As expected, attempts to quantify the ruthenium or rhodium content of the functionalized NPs using energy-dispersive X-ray (EDX) spectroscopy were unsuccessful, as the expected values were below the 1% detection limit.

3.2. Dihydrogen Generation from Water General Procedure

The experimental details of these studies are given in Section 2.2.6, and the results are collected in Table 4. The f-NPs that produced dihydrogen showed the characteristic red color of a $\{\text{Ru}(\text{bpy})_3\}^{2+}$ chromophore, while f-NPs that were either grey or black either did

not produce H₂ or did so with low efficiency. BaTiO₃ NPs and SrTiO₃ NPs activated with H₂O₂, functionalized with ligand **1** and then complexed with RuCl₃·3H₂O and RhCl₃·3H₂O were less active for water reduction. This indicates minimal or no formation of the required photocatalyst(s) on the surface.

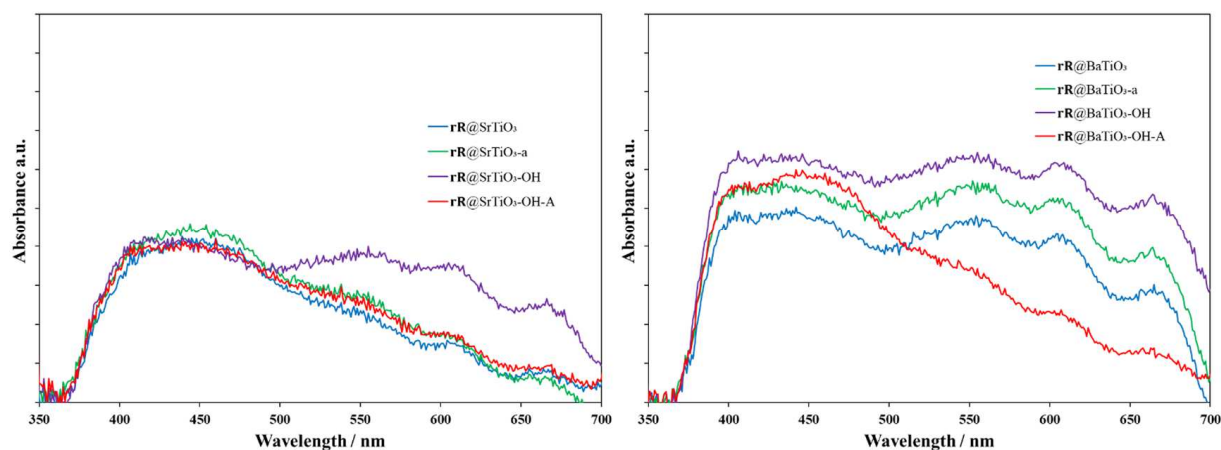


Figure 9. Solid-state absorption spectra of rR@SrTiO₃ NPs (left, blue), rR@SrTiO₃-a NPs (left, green), rR@SrTiO₃-OH NPs (left, violet), rR@SrTiO₃-OH-A NPs (left, red); rR@BaTiO₃ NPs (right, blue), rR@BaTiO₃-a NPs (right, green), rR@BaTiO₃-OH NPs (right, violet), rR@BaTiO₃-OH-A NPs (right, red).

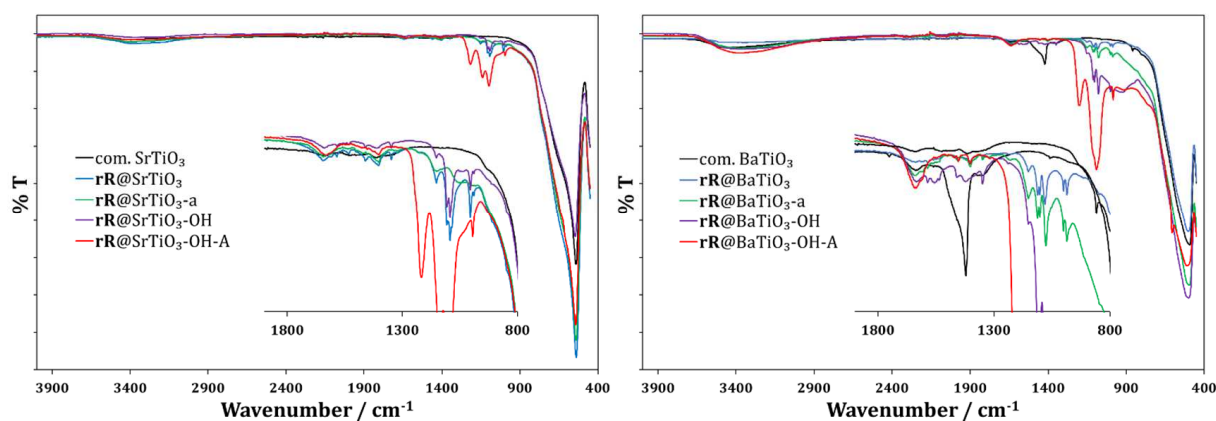


Figure 10. FTIR spectra of rR@SrTiO₃ NPs (left, blue), rR@SrTiO₃-a NPs (left, green), rR@SrTiO₃-OH NPs (left, violet), rR@SrTiO₃-OH-A NPs (left, red); rR@BaTiO₃ NPs (right, blue), rR@BaTiO₃-a NPs (right, green), rR@BaTiO₃-OH NPs (right, violet), rR@BaTiO₃-OH-A NPs (right, red).

Table 4. Dihydrogen-generating experiments.

Entry	GCI ^a /a.u.	H ₂ /mL	Rate /mL h ⁻¹
rR@SrTiO ₃	150,100	3.10	0.77
rR@SrTiO ₃ -a	216,900	4.47	1.12
rR@SrTiO ₃ -OH	31,800	0.66	0.16
rR@SrTiO ₃ -OH-A	94,900	1.96	0.49
rR@BaTiO ₃	43,800	0.90	0.23
rR@BaTiO ₃ -a	90,000	1.86	0.46
rR@BaTiO ₃ -OH	0	0	0
rR@BaTiO ₃ -OH-A	108,600	2.24	0.56

^a GC integral (GCI) was adjusted for pre-existing nitrogen headspace in the reaction vial and partial sampling during the GC measurement.

As discussed in our previous paper [20], surface functionalization is increased by the HNO₃ treatment, leading to more active catalytic sites on the surface and greater hydrogen production.

4. Conclusions

We explored activation methods for SrTiO₃ and BaTiO₃ NPs using H₂O₂ and aqueous HNO₃. Pristine and activated SrTiO₃ and BaTiO₃ NPs were functionalized with anchoring ligand **1** and subsequently elaborated using RuCl₃·3H₂O and bpy, RhCl₃·3H₂O and bpy, or RuCl₃·3H₂O. The potentially photo- and redox-active Rh and Ru surface-bound metal complex f-NPs were used in a photochemical system for the solar generation of H₂ from water. BaTiO₃ NPs and SrTiO₃ NPs activated with H₂O₂, functionalized with ligand **1**, and then complexed with RuCl₃·3H₂O and RhCl₃·3H₂O yielded f-NPs that were inactive for water reduction. **rR@SrTiO₃-a** was the most efficient within our tested materials, giving 1.1 mL H₂ per hour, with **rR@SrTiO₃** being roughly two-thirds as efficient. The complexation of the metal species to the H₂O₂-activated and ligand-functionalized NPs was modified by adjusting the pH to 1.5 with aqueous H₂SO₄. The resulting orange SrTiO₃ and BaTiO₃ NPs were active for water reduction and produced H₂. **rR@SrTiO₃-OH-A** were considerably less active than **rR@SrTiO₃** or **rR@SrTiO₃-a**, while **rR@BaTiO₃-OH-A** performed better than **rR@BaTiO₃-a**. Hence, pH seems to be more important during complexation than previously thought, and adjusting it can play a major role. It is unclear if the drop in efficiency for **rR@SrTiO₃-OH-A** was due to residual H₂SO₄ influencing the pH of the suspension during the water reduction or if complexation was impacted. For **rR@BaTiO₃-OH-A**, the solid-state absorption spectroscopic data and the red color of the functionalized NPs further suggest the formation of surface-bound {Ru(bpy)₃}²⁺ chromophores.

We conclude that extensively functionalized SrTiO₃ or BaTiO₃ NPs may perform better than TiO₂ NPs for water reduction. However, the former NPs are more expensive than TiO₂, and cost-benefit and scale-up limitations should be explored. Particle size might also play a significant role in surface loading, and we note that the pristine BaTiO₃ and SrTiO₃ NPs had 2 to 4 times larger radii than the TiO₂ NPs. This work included the characterization of activated f-NPs and metal complex f-NPs using FTIR spectroscopy, solid-state absorption spectroscopy, and TGA-MS, providing evidence for successful functionalization.

Supplementary Materials: The following supporting information can be downloaded at: <https://www.mdpi.com/article/10.3390/nano13142094/s1>. Details of instrumentation and procedure, characterization details. Figures S1–S4: TGA and TGA-MS spectra for pristine NPs (SrTiO₃, BaTiO₃). Figures S5–S7: TGA and TGA-MS spectra for acid-activated NPs (SrTiO₃-a, BaTiO₃-a). Figures S8–S11: TGA and TGA-MS spectra for H₂O₂-activated NPs (SrTiO₃-OH, BaTiO₃-OH). Figures S12–S17: TGA, TGA-MS, and MALDI spectra for pristine with ligand **1**-functionalized NPs (**1@SrTiO₃**, **1@BaTiO₃**). Figures S18–S22: TGA, TGA-MS, and MALDI spectra for acid-activated with ligand **1**-functionalized NPs (**1@SrTiO₃-a**, **1@BaTiO₃-a**). Figures S23–S28: TGA, TGA-MS, and MALDI spectra for H₂O₂-activated with ligand **1**-functionalized NPs (**1@SrTiO₃-OH**, **1@BaTiO₃-OH**). Figures S29–S35: TGA, TGA-MS, and MALDI spectra for pristine with ligand **1**-functionalized NPs and ruthenium- and bpy-complexed NPs (**Ru@SrTiO₃**, **Ru@BaTiO₃**). Figures S36–S40: TGA, TGA-MS, and MALDI spectra for pristine with ligand **1**-functionalized NPs and ruthenium-, rhodium-, and bpy-complexed NPs (**rR@SrTiO₃**, **rR@BaTiO₃**). Figure S41–S45: TGA, TGA-MS, and MALDI spectra for acid-activated with ligand **1**-functionalized NPs and ruthenium-, rhodium-, and bpy-complexed NPs (**rR@SrTiO₃-a**, **rR@BaTiO₃-a**). Figures S46–S51: TGA, TGA-MS, and MALDI spectra for H₂O₂-activated with ligand **1**-functionalized NPs and ruthenium-, rhodium-, and bpy-complexed NPs (**rR@SrTiO₃-OH**, **rR@BaTiO₃-OH**). Figures S52–S55: TGA and MALDI spectra for H₂O₂-activated with ligand **1**-functionalized NPs and under adjusted pH with ruthenium-, rhodium-, and bpy-complexed NPs (**rR@SrTiO₃-OH-A**, **rR@BaTiO₃-OH-A**) Figure S56. FTIR spectra of commercial SrTiO₃ NPs mixed with aqueous H₂SO₄.

Author Contributions: Methodology, investigation, formal analysis, writing of original draft: S.A.F.; manuscript, review and editing: C.E.H. and E.C.C.; supervision, project management, funding acquisition: C.E.H. and E.C.C. All authors have read and agreed to the published version of the manuscript.

Funding: This research was funded by the University of Basel.

Data Availability Statement: Data are available from the authors upon request.

Acknowledgments: We acknowledge support from the University of Basel.

Conflicts of Interest: The authors declare no conflict of interest.

References

1. Available online: <https://www.ipcc.ch/sr15/download/#full> (accessed on 4 November 2022).
2. Available online: <https://www.giss.nasa.gov/projects/impacts/> (accessed on 4 November 2022).
3. Available online: <https://climate.nasa.gov/news/2865/a-degree-of-concern-why-global-temperatures-matter> (accessed on 4 November 2022).
4. Solomon, S.; Plattner, G.-K.; Knutti, R.; Friedlingstein, P. Irreversible climate change due to carbon dioxide emissions. *Proc. Natl. Acad. Sci. USA* **2009**, *106*, 1704–1709. [[CrossRef](#)] [[PubMed](#)]
5. Raftery, A.E.; Zimmer, A.; Frierson, D.M.W.; Startz, R.; Liu, P. Less than 2 °C warming by 2100 unlikely. *Nat. Clim. Change* **2017**, *7*, 637–641. [[CrossRef](#)] [[PubMed](#)]
6. Kang, J.-N.; Wei, Y.-M.; Liu, L.-C.; Han, R.; Yu, B.-Y.; Wang, J.-W. Energy systems for climate change mitigation: A systematic review. *Appl. Energy* **2020**, *263*, 114602. [[CrossRef](#)]
7. Rivard, E.; Trudeau, M.; Zaghbi, K. Hydrogen Storage for Mobility: A Review. *Materials* **2019**, *12*, 1973. [[CrossRef](#)]
8. Johnson, T.C.; Morris, D.J.; Wills, M. Hydrogen generation from formic acid and alcohols using homogeneous catalysts. *Chem. Soc. Rev.* **2010**, *39*, 81–88. [[CrossRef](#)]
9. Chen, S.; Takata, T.; Domen, K. Particulate photocatalysts for overall water splitting. *Nat. Rev. Mater.* **2017**, *2*, 17050. [[CrossRef](#)]
10. Mei, B.; Han, K.; Mul, G. Driving Surface Redox Reactions in Heterogeneous Photocatalysis: The Active State of Illuminated Semiconductor-Supported Nanoparticles during Overall Water-Splitting. *ACS Catal.* **2018**, *8*, 9154–9164. [[CrossRef](#)]
11. Chen, Y.; Wang, M.; Xiang, S.; Liu, J.; Feng, S.; Wang, C.; Zhang, N.; Feng, T.; Yang, M.; Zhang, K.; et al. Hierarchical Hollow Nanocages Derived from Polymer/Cobalt Complexes for Electrochemical Overall Water Splitting. *ACS Sustain. Chem. Eng.* **2019**, *7*, 10912–10919. [[CrossRef](#)]
12. Wang, Z.; Li, C.; Domen, K. Recent developments in heterogeneous photocatalysts for solar-driven overall water splitting. *Chem. Soc. Rev.* **2019**, *48*, 2109–2125. [[CrossRef](#)]
13. Maleki, A.; Taheri-Ledari, R.; Ghalavand, R.; Firouzi-Haji, R. Palladium-decorated o-phenylenediamine-functionalized Fe₃O₄/SiO₂ magnetic nanoparticles: A promising solid-state catalytic system used for Suzuki–Miyaura coupling reactions. *J. Phys. Chem.* **2020**, *136*, 109200. [[CrossRef](#)]
14. Hassan, A.F.; Elhadidy, H. Effect of Zr⁴⁺ doping on characteristics and sonocatalytic activity of TiO₂/carbon nanotubes composite catalyst for degradation of chlorpyrifos. *J. Phys. Chem.* **2019**, *129*, 180–187. [[CrossRef](#)]
15. Sajjadi, S.; Khataee, A.; Darvishi Cheshmeh Soltani, R.; Hasanzadeh, A. N, S co-doped graphene quantum dot-decorated Fe₃O₄ nanostructures: Preparation, characterization and catalytic activity. *J. Phys. Chem.* **2019**, *127*, 140–150. [[CrossRef](#)]
16. Stevens, P.D.; Fan, J.; Gardimalla, H.M.R.; Yen, M.; Gao, Y. Superparamagnetic Nanoparticle-Supported Catalysis of Suzuki Cross-Coupling Reactions. *Org. Lett.* **2005**, *7*, 2085–2088. [[CrossRef](#)] [[PubMed](#)]
17. Adriano Zecchina, S.B.; Groppo, E. *Selective Nanocatalysts and Nanoscience: Concepts for Heterogeneous and Homogeneous Catalysis*; Wiley: Weinheim, Germany, 2011.
18. Samira Bagheri, N.M.J. *Nanocatalysts in Environmental Applications*; Springer: Cham, Switzerland, 2018.
19. Albonetti, S.; Mazzoni, R.; Cavani, F. Ch. 1 Homogeneous, Heterogeneous and Nanocatalysis. In *Transition Metal Catalysis in Aerobic Alcohol Oxidation*; Cardona, F., Parmeggiani, C., Eds.; Green Chemistry Series; RSC: New York, NY, USA, 2015; pp. 1–39.
20. Freimann, S.A.; Housecroft, C.E.; Constable, E.C. Attraction in Action: Reduction of Water to Dihydrogen Using Surface-Functionalized TiO₂ Nanoparticles. *Nanomaterials* **2022**, *12*, 789. [[CrossRef](#)] [[PubMed](#)]
21. Emsley, J. *The Elements*, 3rd ed.; Oxford University Press Inc.: New York, NY, USA, 1994.
22. Available online: <https://pubs.usgs.gov/pp/0440d/report.pdf> (accessed on 17 October 2022).
23. Ober, J.A.; McRae, M.E.; Gambogi, J. *Mineral Commodity Summaries 2021*; U.S. Geological Survey: Reston, VA, USA, 2021; p. 200.
24. Konstas, P.-S.; Konstantinou, I.; Petrakis, D.; Albanis, T. Development of SrTiO₃ Photocatalysts with Visible Light Response Using Amino Acids as Dopant Sources for the Degradation of Organic Pollutants in Aqueous Systems. *Catalysts* **2018**, *8*, 528. [[CrossRef](#)]
25. Kappadan, S.; Gebreab, T.W.; Thomas, S.; Kalarikkal, N. Tetragonal BaTiO₃ nanoparticles: An efficient photocatalyst for the degradation of organic pollutants. *Mater. Sci. Semicond. Process* **2016**, *51*, 42–47. [[CrossRef](#)]
26. Xiong, X.; Tian, R.; Lin, X.; Chu, D.; Li, S. Formation and Photocatalytic Activity of BaTiO₃ Nanocubes via Hydrothermal Process. *J. Nanomater.* **2015**, *2015*, 692182. [[CrossRef](#)]
27. Konta, R.; Ishii, T.; Kato, H.; Kudo, A. Photocatalytic Activities of Noble Metal Ion Doped SrTiO₃ under Visible Light Irradiation. *J. Phys. Chem. B* **2004**, *108*, 8992–8995. [[CrossRef](#)]
28. Rohj, R.K.; Hossain, A.; Mahadevan, P.; Sarma, D.D. Band Gap Reduction in Ferroelectric BaTiO₃ through Heterovalent Cu-Te Co-Doping for Visible-Light Photocatalysis. *Front. Chem.* **2021**, *9*, 682979. [[CrossRef](#)]

29. Chen, P.; Li, X.; Ren, Z.; Wu, J.; Li, Y.; Liu, W.; Li, P.; Fu, Y.; Ma, J. Enhancing Photocatalysis of Ag Nanoparticles Decorated BaTiO₃ Nanofibers through Plasmon-Induced Resonance Energy Transfer Turned by Piezoelectric Field. *Catalysts* **2022**, *12*, 987. [CrossRef]
30. Ma, L.; Sun, T.; Cai, H.; Zhou, Z.-Q.; Sun, J.; Lu, M. Enhancing photocatalysis in SrTiO₃ by using Ag nanoparticles: A two-step excitation model for surface plasmon-enhanced photocatalysis. *J. Chem. Phys.* **2015**, *143*, 084706. [CrossRef] [PubMed]
31. Jiang, J.; Kato, K.; Fujimori, H.; Yamakata, A.; Sakata, Y. Investigation on the highly active SrTiO₃ photocatalyst toward overall H₂O splitting by doping Na ion. *J. Catal.* **2020**, *390*, 81–89. [CrossRef]
32. Lyu, H.; Hisatomi, T.; Goto, Y.; Yoshida, M.; Higashi, T.; Katayama, M.; Takata, T.; Minegishi, T.; Nishiyama, H.; Yamada, T.; et al. An Al-doped SrTiO₃ photocatalyst maintaining sunlight-driven overall water splitting activity for over 1000 h of constant illumination. *Chem. Sci.* **2019**, *10*, 3196–3201. [CrossRef]
33. Alex, K.V.; Prabhakaran, A.; Jayakrishnan, A.R.; Kamakshi, K.; Silva, J.P.B.; Sekhar, K.C. Charge Coupling Enhanced Photocatalytic Activity of BaTiO₃/MoO₃ Heterostructures. *ACS Appl. Mater. Interfaces* **2019**, *11*, 40114–40124. [CrossRef] [PubMed]
34. Fazli, A.; Zakeri, F.; Khataee, A.; Orooji, Y. A BaTiO₃/WS₂ composite for piezo-photocatalytic persulfate activation and ofloxacin degradation. *Commun. Chem.* **2022**, *5*, 95. [CrossRef]
35. Yadav, A.A.; Hunge, Y.M.; Mathe, V.L.; Kulkarni, S.B. Photocatalytic degradation of salicylic acid using BaTiO₃ photocatalyst under ultraviolet light illumination. *J. Mater. Sci. Mater.* **2018**, *29*, 15069–15073. [CrossRef]
36. Kato, K.; Jiang, J.; Sakata, Y.; Yamakata, A. Effect of Na-Doping on Electron Decay Kinetics in SrTiO₃ Photocatalyst. *ChemCatChem* **2019**, *11*, 6349–6354. [CrossRef]
37. Qin, Y.; Fang, F.; Xie, Z.; Lin, H.; Zhang, K.; Yu, X.; Chang, K. La,Al-Codoped SrTiO₃ as a Photocatalyst in Overall Water Splitting: Significant Surface Engineering Effects on Defect Engineering. *ACS Catal.* **2021**, *11*, 11429–11439. [CrossRef]
38. Moss, B.; Wang, Q.; Butler, K.T.; Grau-Crespo, R.; Selim, S.; Regoutz, A.; Hisatomi, T.; Godin, R.; Payne, D.J.; Kafizas, A.; et al. Linking in situ charge accumulation to electronic structure in doped SrTiO₃ reveals design principles for hydrogen-evolving photocatalysts. *Nat. Mater.* **2021**, *20*, 511–517. [CrossRef]
39. Fan, Y.; Liu, Y.; Cui, H.; Wang, W.; Shang, Q.; Shi, X.; Cui, G.; Tang, B. Photocatalytic Overall Water Splitting by SrTiO₃ with Surface Oxygen Vacancies. *Nanomaterials* **2020**, *10*, 2572. [CrossRef]
40. Maeda, K. Rhodium-Doped Barium Titanate Perovskite as a Stable p-Type Semiconductor Photocatalyst for Hydrogen Evolution under Visible Light. *ACS Appl. Mater. Interfaces* **2014**, *6*, 2167–2173. [CrossRef]
41. Fujisawa, J.-I.; Eda, T.; Hanaya, M. Comparative study of conduction-band and valence-band edges of TiO₂, SrTiO₃, and BaTiO₃ by ionization potential measurements. *Chem. Phys. Lett.* **2017**, *685*, 23–26. [CrossRef]
42. Liao, D.L.; Wu, G.S.; Liao, B.Q. Zeta potential of shape-controlled TiO₂ nanoparticles with surfactants. *Colloids Surf.* **2009**, *348*, 270–275. [CrossRef]
43. Bhagya, N.P.; Prashanth, P.A.; Raveendra, R.S.; Sathyanarayani, S.; Ananda, S.; Nagabhushana, B.M.; Nagabhushana, H. Adsorption of hazardous cationic dye onto the combustion derived SrTiO₃ nanoparticles: Kinetic and isotherm studies. *J. Asian Ceram. Soc.* **2016**, *4*, 68–74. [CrossRef]
44. Cai, J.; Wei, H.; Zhang, Y.; Cai, R.; Zhang, X.; Wang, Y.; Liu, J.; Tan, H.H.; Xie, T.; Wu, Y. Designed Construction of SrTiO₃/SrSO₄/Pt Heterojunctions with Boosted Photocatalytic H₂ Evolution Activity. *Eur. J. Chem.* **2021**, *27*, 7300–7306. [CrossRef]
45. Olhero, S.M.; Kaushal, A.; Ferreira, J.M.F. Preventing hydrolysis of BaTiO₃ powders during aqueous processing and of bulk ceramics after sintering. *J. Eur. Ceram. Soc.* **2015**, *35*, 2471–2478. [CrossRef]
46. Luan, W.; Gao, L. Influence of pH value on properties of nanocrystalline BaTiO₃ powder. *Ceram. Int.* **2001**, *27*, 645–648. [CrossRef]
47. Ye, H.-J.; Shao, W.-Z.; Zhen, L. Tetradecylphosphonic acid modified BaTiO₃ nanoparticles and its nanocomposite. *Colloids Surf. A Physicochem. Eng. Asp.* **2013**, *427*, 19–25. [CrossRef]
48. Rechberger, F.; Ilari, G.; Willa, C.; Tervoort, E.; Niederberger, M. Processing of Cr doped SrTiO₃ nanoparticles into high surface area aerogels and thin films. *Mater. Chem. Front.* **2017**, *1*, 1662–1667. [CrossRef]
49. Čulić-Viskota, J.; Dempsey, W.P.; Fraser, S.E.; Pantazis, P. Surface functionalization of barium titanate SHG nanoprobe for in vivo imaging in zebrafish. *Nat. Protoc.* **2012**, *7*, 1618–1633. [CrossRef]
50. Pujari, S.P.; Scheres, L.; Marcelis, A.T.M.; Zuilhof, H. Covalent Surface Modification of Oxide Surfaces. *Angew. Chem. Int. Ed. Engl.* **2014**, *53*, 6322–6356. [CrossRef] [PubMed]
51. Kim, B.; Park, S.W.; Kim, J.-Y.; Yoo, K.; Lee, J.A.; Lee, M.-W.; Lee, D.-K.; Kim, J.Y.; Kim, B.; Kim, H.; et al. Rapid Dye Adsorption via Surface Modification of TiO₂ Photoanodes for Dye-Sensitized Solar Cells. *ACS Appl. Mater. Interfaces* **2013**, *5*, 5201–5207. [CrossRef] [PubMed]
52. Freimann, S.A.; Zare, D.; Housecroft, C.E.; Constable, E.C. The SALSAC approach: Comparing the reactivity of solvent-dispersed nanoparticles with nanoparticulate surfaces. *Nanoscale Adv.* **2020**, *2*, 679–690. [CrossRef] [PubMed]
53. Freimann, S.A.; Prescimone, A.; Housecroft, C.E.; Constable, E.C. Turning over on sticky balls: Preparation and catalytic studies of surface-functionalized TiO₂ nanoparticles. *RSC Adv.* **2021**, *11*, 5537–5547. [CrossRef]
54. Available online: <https://webbook.nist.gov/cgi/cbook.cgi?ID=C7664939&Mask=200#Mass-Spec> (accessed on 17 October 2022).

Disclaimer/Publisher's Note: The statements, opinions and data contained in all publications are solely those of the individual author(s) and contributor(s) and not of MDPI and/or the editor(s). MDPI and/or the editor(s) disclaim responsibility for any injury to people or property resulting from any ideas, methods, instructions or products referred to in the content.